



# Oxygen-vacancy defect engineering to boost the aerobic oxidation of limonene over $\text{Co}_3\text{O}_4$ nanocubes

Jiangyong Liu<sup>a,\*</sup>, Hui Tang<sup>a</sup>, Panming Jian<sup>a</sup>, Bing Liu<sup>b,\*</sup>

<sup>a</sup> School of Chemistry and Chemical Engineering, Yangzhou University, Yangzhou, Jiangsu 225002, China

<sup>b</sup> School of Chemical and Material Engineering, Jiangnan University, Wuxi, Jiangsu 214122, China

## ARTICLE INFO

### Keywords:

$\text{Co}_3\text{O}_4$   
Oxygen vacancy  
Defect engineering  
Limonene  
Oxidation

## ABSTRACT

The heterogeneous aerobic oxidation of biomass-derived limonene under mild reaction conditions is an attractive target for the synthesis of valuable oxygenates, but qualifying catalyst represents an enormous challenge. Herein, we propose an oxygen-vacancy defect engineering strategy for steering the limonene oxidation catalysis over  $\text{Co}_3\text{O}_4$  nanocubes. Comprehensive characterizations demonstrate that the incorporation of oxygen vacancy (Ov) in the  $\text{Co}_3\text{O}_4$  structure triggers the redistribution of charge density and the modulation of Co chemical environment with the formation of more coordinated unsaturated Co atoms. Both the experimental findings and density functional theory (DFT) calculations explicitly evidence the boosting role of Ov in facilitating the radical initiation process, thereby substantially driving the generation of active radicals for the subsequent oxidation to proceed more feasibly. This work paves a way to structural microenvironment modulation induced by oxygen-vacancy defect engineering strategy towards high-performance limonene oxidation catalysis and beyond.

## 1. Introduction

The use of biomass-based derivatives for the synthesis of high value-added chemicals can significantly reduce our dependence on non-renewable fossil fuels, helping to alleviate the energy crisis, protect the environment, and mitigate climate change. As a cyclic monoterpene, limonene has been widely found in more than 300 plant species and some bacteria, with its production of about 70 kt per year (mostly extracted from citrus peel wastes) and market size estimated to surpass 1.9 billion USD by 2024 [1,2]. The oxidation of limonene can produce several important oxygenated derivatives including limonene oxides (limonene monoepoxide and limonene diepoxide), carvone, carveol and perillyl alcohol, which have found wide applications in the food, pharmaceuticals, cosmetics and polymers industries. Thereinto, 1,2-limonene oxide (LO) is a versatile building block for the production of bio-based polycarbonates via copolymerization with  $\text{CO}_2$ , which offers potential alternatives to traditional petroleum-based polymers [3,4].

Preliminary explorations have attempted the homogeneous oxidation of limonene in the presence of various metal complexes as catalysts, such as salen manganese (III) complexes [5],  $\text{PdCl}_2\text{-CuCl}_2$  [6], iron-bipyridine complexes ( $[\text{Fe}^{\text{II}}(\text{bpy})_2]^+ \text{sol}$  and  $[\text{Fe}^{\text{III}}(\text{bpy})_2]^+ \text{sol}$ ) [7], amphiphilized metalloporphyrins [8], polyoxotungstate

( $\text{Na}_{10}[\text{Co}_5\text{W}_{19}\text{O}_{70}\text{H}_4] \cdot 44\text{H}_2\text{O}$ ) [9], and  $[\text{MoO}_2\text{L}]_2$  with salicylidene amino(thio)phenolate ligands [10]. Despite the easily accessible active sites provided by the metal complexes, the homogeneous catalytic systems suffer from insurmountable obstacles of catalyst separation and recovery in the recycling tests. Immobilization of the homogeneous metal complexes onto solid supports have been adopted to overcome these limitations/problems. Typical catalysts for this strategy include manganese acetylacetonate complex anchored on MCM-41 [11], carbon anchored transition metal Schiff base complexes [12], supported Keggin heteropolycompounds [13], silica functionalized with silylated Ti-salicylaldimine complex [14], iron phthalocyanine complex  $\text{FePcCl}_{16}$  immobilized on amino-modified silica [15], zeolite-Y entrapped oxovanadium (IV) complexes [16] and Ru(III) and Fe(III) complexes [17], Mn(Salen) complexes immobilized on sulfonic acid-functionalized SBA-15 molecular sieves [18] and 3-hydroxypropyltrimethylsilyl functionalized MCM-41 [19]. However, it's still a great challenge to avoid metal leaching during the reaction process, leading to declined catalytic stability, deteriorated performance and degradation of products. Additionally, the expensive precursors and complicated and time-consuming procedures needed for the preparation of these catalysts impede their development for scalable applications. Therefore, based on a recycle/reuse principle, recent studies have directed towards the

\* Corresponding authors.

E-mail addresses: [liujy@yzu.edu.cn](mailto:liujy@yzu.edu.cn) (J. Liu), [liubing@jiangnan.edu.cn](mailto:liubing@jiangnan.edu.cn) (B. Liu).

<https://doi.org/10.1016/j.apcatb.2023.122828>

Received 22 February 2023; Received in revised form 18 April 2023; Accepted 29 April 2023

Available online 1 May 2023

0926-3373/© 2023 Elsevier B.V. All rights reserved.

heterogeneous oxidation of limonene in the presence of solid catalysts, including V-MCM-41 [20], activated carbon [21,22], carbon-supported ruthenium [23], palladium supported on hydrotalcites [24],  $\text{V}_2\text{O}_5/\text{Al}_2\text{O}_3\text{-MgO}$  [25], Fe/nanoporous carbon [26,27], cobalt doped mesoporous silica [28], Ti-MCM-41 [29,30] and TS-1 [31]. Noticeably, most of these studies use  $\text{H}_2\text{O}_2$  or tert-butyl hydroperoxide as the oxidants. From the environmental and industrial perspectives, molecular oxygen is an ideal oxidant due to its natural, cheap and environmentally friendly properties, emerging broad prospects for industry and academia [32,33]. Hence, it can be deduced that the heterogeneous oxidation of limonene with molecular oxygen as oxidant is more promising. However, it remains far from fully investigated to date. In this area, the major challenge lies in the development of highly active and selective catalysts that can be easily prepared from earth-abundant elements, and ongoing research is required.

Based on these understandings, the challenges motivate us to exploit a good catalyst for limonene oxidation. Herein, oxygen vacancy-enriched  $\text{Co}_3\text{O}_4$  cubes (OVCC) were developed via a facile liquid-phase reduction treatment of the pristine  $\text{Co}_3\text{O}_4$  cubes (PCC) (Scheme 1). The modified surface was investigated by using a combination of advanced characterization techniques including X-ray photoelectron spectroscopy (XPS), X-ray absorption near edge structure (XANES) and extended X-ray absorption fine structure (EXAFS) spectroscopy. This defect engineering strategy is demonstrated to be effective in tuning the electronic configuration of  $\text{Co}_3\text{O}_4$  by introducing Ov defects, thereby remarkably boosting the limonene oxidation catalysis. Experimental results combined with theoretical calculations reveal that the enhanced performance stems from the facilitated adsorption/activation of  $\text{O}_2$  and isobutyraldehyde for the generation of abundant reactive oxygen species by surface manipulation. Furthermore, the adoption of oxygen-vacancy defect engineering strategy for steering the limonene oxidation catalysis can bring several advantages from the practical application aspect, such as facile and economic catalyst preparation process, contributing to the sustainable development by promoting biomass utilization, and production of high-value-added oxygenated chemicals.

## 2. Experimental

### 2.1. Synthesis of the PCC and OVCC catalysts

The PCC was prepared by a facile hydrothermal method. In a typical synthesis, 0.04 mol of  $\text{Co}(\text{NO}_3)_2 \cdot 6\text{H}_2\text{O}$  and 0.04 mol of NaOH were dissolved in 15 mL of deionized water, respectively. Thereafter, the NaOH solution was added into the  $\text{Co}(\text{NO}_3)_2$  solution. After continuous

stirring for 30 min, the mixture was transferred to a stainless steel hydrothermal kettle lined with polytetrafluoroethylene for a hydrothermal treatment at 180 °C for 5 h. After the reaction, the obtained precipitate was separated by filtration, and washed thoroughly with deionized water and ethanol. After drying at 80 °C for 12 h, the obtained precursor was calcined at 500 °C for 2 h. The pristine  $\text{Co}_3\text{O}_4$  nanocubes were thus prepared and labeled as PCC.

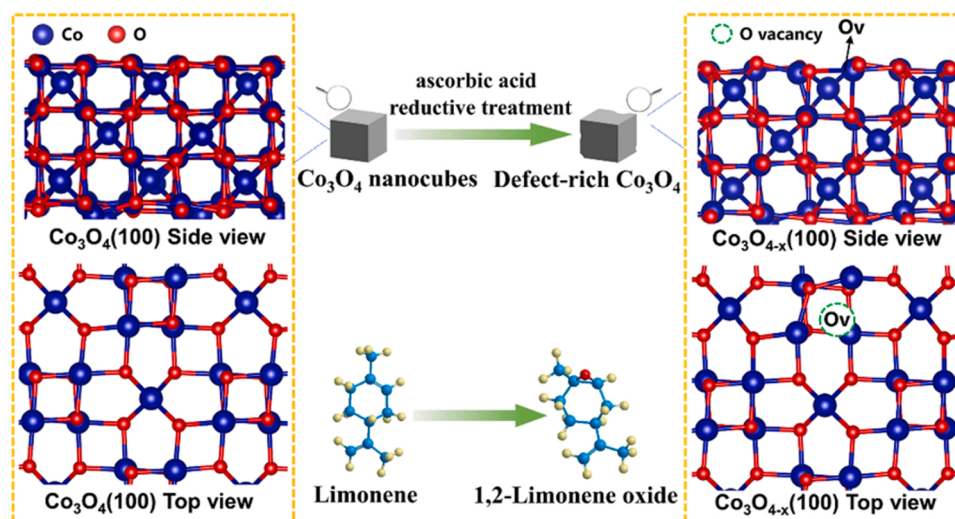
For the preparation of the OVCC catalyst, the as-prepared PCC further underwent a liquid-phase reductive treatment assisted by ascorbic acid. In a typical treatment, 0.35 g of PCC was dispersed in 0.05 mol/L of ascorbic acid solution. The suspension was allowed for stirring for 20 min and then processed for an ultrasonic treatment for 5 min. The obtained powder was washed with deionized water several times, and then dried at 80 °C for 12 h.

### 2.2. Catalyst Characterization

Powder X-ray diffraction (XRD) was carried out using a D8 Advance diffractometer using  $\text{Cu K}\alpha$  radiation. X-ray photoelectron spectroscopy (XPS) was conducted on a Thermo, Fisher Scientific ESCALAB 250Xi spectrometer. The structure and morphologies of the samples were acquired by the scanning electron microscopy (SEM, Hitachi S-4800), transmission electron microscopy (TEM, JEM-2100) and high-resolution TEM (HRTEM, JEM-2100). The EDS measurements were also performed on JEM-2100. The  $\text{N}_2$  adsorption-desorption isotherms were recorded on a Quantachrome Autosorb-iQ3 sorption analyzer. Raman spectra were recorded on a Renishaw inVia laser Raman spectrometer. Electron paramagnetic resonance (EPR) spectra were recorded on a Bruker A300-10/12 spectrometer. The temperature-programmed desorption of oxygen ( $\text{O}_2$ -TPD) experiments were performed on a Micromeritics Autochem II Chemisorption analyzer. In a typical test, 100 mg of sample was pretreated under He ( $50 \text{ mL min}^{-1}$ ) at 300 °C for 1 h, followed by cooling down to 50 °C. Then, the sample was exposed to 10 %  $\text{O}_2/\text{He}$  (vol.) for adsorption of oxygen for 1 h. After purging the system in a He flow, the temperature was raised from 50 to 700 °C at a ramping rate of  $10^\circ\text{C}\cdot\text{min}^{-1}$ . The effluent  $\text{O}_2$  during the process was recorded and analyzed. XAFS (X-ray absorption fine structure) measurements were performed at the BL14W Beam line at the Shanghai Synchrotron Radiation Facility (SSRF) (Shanghai, China).

### 2.3. Catalytic test

In a typical test for the oxidation of limonene, 8 mmol of limonene, 15 mmol of isobutyraldehyde, 10 mL of acetonitrile and 0.15 g of



**Scheme 1.** Schematic illustration of the oxygen-vacancy defect engineering strategy for boosting limonene oxidation catalysis.

catalyst were charged into a high-pressure stainless autoclave. After purging the reactor with oxygen three times, the reactor was sealed and heated to the desired temperature under constant stirring. The reactor was fed with oxygen up to pressure of 0.2 MPa. After reaction for the desired time, the reactor was cooled down naturally and then depressurized. The obtained products were sampled for GC analysis equipped with a FID detector. All experiments were conducted twice to ensure reproducibility. The used catalyst was isolated by centrifugation, washed repeatedly with deionized water and acetone, and then dried at 80 °C for 12 h. The recovered catalyst was then used in the subsequent run for the recycling test.

## 2.4. DFT calculations

The spin-polarized density functional theory (DFT) calculations were performed using the Vienna ab initio simulation package (VASP) [34, 35]. A correction for Coulomb and exchange interactions was employed by setting  $U_{\text{eff}} = 3.5$  eV ( $U_{\text{eff}} = \text{coulomb } U - \text{exchange } J$ ) for Co atoms, using the model proposed by Dudarev et al. [36]. The D3 correction method (DFT-D3) was employed in order to include van der Waals (vdW) interactions [37]. The projector-augmented wave (PAW) method was used to describe the electron-ion interaction [38]. The generalized gradient approximation with the Perdew-Burke-Ernzerhof (GGA-PBE) was used to model the electron exchange correlation [39]. Electron smearing was employed via Gaussian smearing method with a smearing width consistent to 0.05 eV. Valence electrons were described by a plane

wave basis with an energy cutoff of 450 eV. The surface Brillouin was sampled at the  $\Gamma$ -point. Optimized structures were obtained by minimizing the forces on each ion using the conjugate gradient algorithm until  $< 0.03$  eV/Å. The energy convergence criteria was set to  $10^{-5}$  eV.

A cubic  $\text{Co}_2\text{O}_3$  cell with  $Fd\bar{3}m$  space group was used to model the  $\text{Co}_3\text{O}_4$  bulk, containing 8 tetrahedral  $\text{Co}^{2+}$  and 16 octahedral  $\text{Co}^{3+}$  ions. According to Sautet et al.' study [40], the magnetic structure of  $\text{Co}^{2+}$  was set to antiferromagnetic ordering, while  $\text{Co}^{3+}$  has no magnetic moment. The lattice parameter for the  $\text{Co}_2\text{O}_3$  cell was calculated to be 8.09 Å, which matches the experimental values well (8.08 Å) [41]. The magnetic moment of  $\text{Co}^{2+}$  was calculated to be 2.64  $\mu_B$ , which is consistent with Sautet et al.' result [40]. According to the HRTEM characterization results, surface reactions were studied on  $\text{Co}_3\text{O}_4$  (100) surface, which was modeled using a  $\text{Co}_3\text{O}_4$  (100) slab consisting of 48 Co and 64 O atoms and separated by a vacuum of 15 Å in the z direction.

## 3. Results and discussion

### 3.1. Characterizations of catalysts

As illustrated in Fig. 1a,  $\text{Co}_3\text{O}_4$  nanocubes were prepared by a facile one-pot hydrothermal method. After further undergoing a reductive treatment of the  $\text{Co}_3\text{O}_4$  nanocubes assisted by ascorbic acid, the target defective  $\text{Co}_3\text{O}_4$  nanocubes enriched with oxygen vacancies were obtained. For clarity, the samples of pristine  $\text{Co}_3\text{O}_4$  nanocubes and modified  $\text{Co}_3\text{O}_4$  nanocubes were marked as PCC and OVCC, respectively.

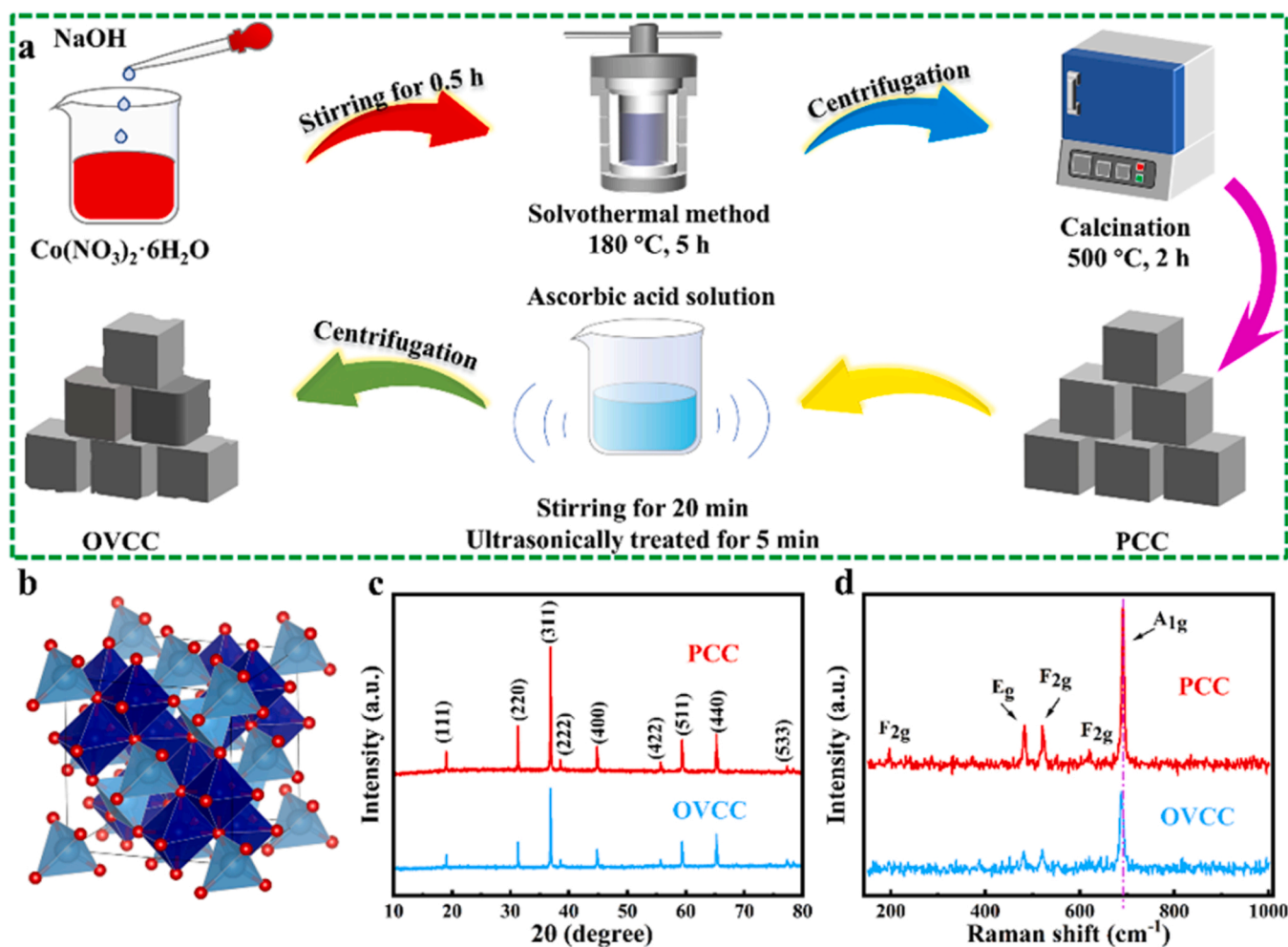


**Fig. 1.** (a) The schematic diagram for the preparation of the PCC and OVCC catalysts. (b) The schematic illustration of the spinel structure of  $\text{Co}_3\text{O}_4$ . XRD (c) and Raman (d) spectra of the samples.



Fig. 1b shows the spinel structure of  $\text{Co}_3\text{O}_4$ , in which Co(II) ions occupy the tetrahedral sites and Co(III) ions are located in octahedral sites [42]. It has been revealed that  $\text{Co}_3\text{O}_4$  as a reducible metal oxide has relatively weak metal–oxygen bond and low hopping barrier for the generation of Ov [43]. Hence, it can be reasonably inferred that under the reducing environment, the removal of oxygen atoms from the surface to form Ov will be accelerated. The crystal structures of the samples were analyzed by XRD as shown in Fig. 1c, suggesting that all the diffraction peaks can match well with the standard spinel  $\text{Co}_3\text{O}_4$  phase (JCPDS No.43–1003). This denotes that the reduction treatment does not alter the crystal structure of  $\text{Co}_3\text{O}_4$ . The only difference is that the OVCC presents lower peak intensity than the PCC, which is possibly caused by the introduction of surface defects after the chemical reduction modification. According to the Scherrer equation, the average crystallite size of the OVCC was calculated to be 47.2 nm, which is slightly smaller than that of the PCC (49.0 nm). The Raman spectra of the samples are presented in Fig. 1d. The Raman active modes at 197, 483, 521, 620 and  $691\text{ cm}^{-1}$  are associated with the  $\text{F}_{2g}^{(1)}$ ,  $\text{E}_g$ ,  $\text{F}_{2g}^{(2)}$ ,  $\text{F}_{2g}^{(3)}$  and  $\text{A}_{1g}$  vibration of the  $\text{Co}_3\text{O}_4$  spinel structure, respectively [44,45]. Compared with the PCC, the OVCC displays lower peak intensity and a shift of peak position, demonstrating the intensified lattice distortion with weakened Co–O bonds and more Ov generated, resulting from the effective defect-assisted surface modification [46,47].

As exhibited in the SEM images (Fig. 2(a, b)) and TEM image (Fig. 2c), the PCC is composed of uniformly dispersed  $\text{Co}_3\text{O}_4$  nanocubes with an average size of 100–200 nm. The OVCC inherits the cube-like character of the PCC as displayed in the SEM images in Fig. 2(d, e) and TEM image in Fig. 2f, while the shape of the nanocubes is somewhat irregular with the surface and edges seemed to be disordered. This decrease in shape uniformity can be attributed to the chemical etching of the initial nanocubes during the reduction process, which may be an implication of the presence of surface defects. The EDS analysis (Fig. S1) show the composite elements of Co and O, which are homogeneously distributed as observed from the EDS mapping images of one single nanocube in the OVCC shown in Fig. 2(g–i). The HRTEM images in Fig. 2(j, k) show that both samples exhibit lattice fringes ascribed to the (220) planes of the spinel  $\text{Co}_3\text{O}_4$ . The two sets of mutually perpendicular (220) crystal planes suggest a (100) surface of the  $\text{Co}_3\text{O}_4$  nanocube, which is in accordance with the previous report that bulk  $\text{Co}_3\text{O}_4$  cube tends to possess a preferential (100) surface [48]. The corresponding selected area electron diffraction (SAED) pattern of the OVCC in Fig. 2l shows a polycrystalline feature.

More information regarding the structure of the samples were detected by the  $\text{N}_2$  adsorption–desorption test. As presented in Fig. 3a, both samples show similar adsorption–desorption profiles, in which the obvious hysteresis loops suggest their mesoporous character. As a result, similar specific surface area determined from the Brunauer–Emmett–Teller (BET) method and same average pore size measured from the Barrett–Joyner–Halenda (BJH) method (Fig. 3b) are obtained for the two samples (PCC:  $4.7\text{ m}^2\text{ g}^{-1}$ , 3.1 nm; OVCC:  $4.6\text{ m}^2\text{ g}^{-1}$ , 3.1 nm). All these findings further indicate that the texture and morphology maintained before and after the reduction treatment. XPS was carried out to probe the surface composition and chemical bonding states of the samples. As depicted in Fig. 3c, two elements of Co and O are detected for both samples, with the presence of C attributable to the hydrocarbon contaminants in the test. The high-resolution XPS Co 2p in Fig. 3(d, e) present two broad signals of Co  $2p_{3/2}$  and Co  $2p_{1/2}$  and two typical shake-up satellite peaks. The Co  $2p_{3/2}$  and Co  $2p_{1/2}$  signals can be deconvoluted into two components assignable to  $\text{Co}^{3+}$  ( $\sim 779.7$  and  $794.8\text{ eV}$ ) and  $\text{Co}^{2+}$  ( $\sim 781.2$  and  $796.5\text{ eV}$ ) [49]. Based on the area of the XPS fitting results, the atomic ratio of  $\text{Co}^{2+}/\text{Co}^{3+}$  can be measured. While the PCC has a  $\text{Co}^{2+}/\text{Co}^{3+}$  ratio of 0.46, the OVCC presents a much higher  $\text{Co}^{2+}/\text{Co}^{3+}$  ratio of 0.74, suggesting the OVCC with more surface  $\text{Co}^{2+}$ . This is an implication that more surface Ov would be generated in the OVCC in order to maintain the charge balance. Additional information with respect to the oxygen species can be acquired from the

high-resolution XPS O 1s spectra exhibited in Fig. 3(f, g), which can be resolved into three components corresponding to crystal lattice oxygen ( $\text{O}_1$ ,  $\sim 530.1\text{ eV}$ ), surface adsorbed oxygen near Ov site ( $\text{O}_2$ ,  $\sim 531.2\text{ eV}$ ) and adsorbed hydroxyl species ( $\text{O}_3$ ,  $\sim 533.0\text{ eV}$ ) [50,51]. Obviously, the OVCC presents higher relative intensity of  $\text{O}_2$  species when compared with the PCC. The remarkably larger  $\text{O}_2/\text{O}_1$  ratio of 0.66 for the OVCC (0.24 for the PCC) consolidates its higher concentration of Ov.

EPR was further employed to validate the enhanced creation of Ov in the OVCC since this technology is sensitive to paramagnetic species involving unpaired electrons [52]. The signal with a g factor of 2.003 (Fig. 3h) can be attributed to the singly ionized Ov originated from the delocalized electrons. As expected, the OVCC possesses an apparently stronger EPR signal than the PCC, further affirming the higher concentration of Ov in the former [53,54]. All these results collectively substantiate that with the assistance of the reduction treatment, the formation of Ov defects in the  $\text{Co}_3\text{O}_4$  nanocubes becomes much easier. The properties of oxygen species in the catalysts were further explored via the  $\text{O}_2$ -TPD experiments. As displayed in Fig. 3i, the desorption profiles for both samples can be classified into three regions: the region located below  $180^\circ\text{C}$  (I) is attributed to the desorption of surface adsorbed oxygen species; the region within the scope of  $180$ – $530^\circ\text{C}$  (II) is assigned to the desorption of surface lattice oxygen species; the region higher than  $530^\circ\text{C}$  corresponds to the desorption of bulk lattice oxygen species (III) [55,56]. For the OVCC, the desorption of  $\text{O}_1$  species appears at a relatively lower temperature, and the desorption area of  $\text{O}_{II}$  species are much larger than that in the PCC. These findings suggest that the OVCC enriched with Ov has good  $\text{O}_2$  adsorption affinity and enhanced oxygen mobility, which is beneficial for the supply of abundant active oxygen species for oxidation of hydrocarbons [57–59].

XAFS (X-ray absorption fine structure) was further performed to determine the fine structure of the  $\text{Co}_3\text{O}_4$  nanocubes. Fig. 4a shows the Co K-edge XANES spectra of the samples. The absorption edge of the OVCC shifts to the lower energy side, indicating a lower Co oxidation state in the OVCC [60], consistent with the above Co 2p XPS findings. The Co K-edge EXAFS curves of the samples are shown in Fig. 4b. The two prominent peaks at  $1.5\text{ \AA}$  and  $2.4\text{ \AA}$  can be attributed to the coordination of Co–O and Co–Co, respectively [61]. Importantly, the peak intensities in the OVCC are lower than that in the PCC, suggesting a lower coordination number in the OVCC [62]. This further demonstrates the increased lattice disorder and presence of more Ov defects and low-coordinated Co sites in the OVCC [43,63]. These findings are consistent with the above discussions. The corresponding EXAFS wavelet transform (WT) analysis results in Fig. 4(c, d) display two intensity maximums assigned to the Co–O and Co–Co backscattering contributions, respectively [64].

### 3.2. Catalytic performance for the limonene oxidation

To demonstrate the positive role of defect engineering strategy in the limonene oxidation catalysis, the tailor-made OVCC was investigated as a potential catalyst for the selective aerobic oxidation of limonene. The PCC was also carried out in the test as a contrast. As depicted in Fig. 5a, the conversion of limonene for the OVCC can reach 87.4 %, which is much higher than that for the PCC (52.7 %), suggesting the high activity of OVCC toward limonene oxidation. For these experiments, LO and limonene diepoxide (LDO) were identified as the two main products, along with small amounts of byproducts (Fig. S2). While the OVCC shows a slightly lower LO selectivity than the PCC (79.6 % vs. 86.3 %), the LO yield of the OVCC achieves 69.6 %, apparently higher than that of the PCC (45.5 %). This suggests that the OVCC with enriched Ov is an efficient catalyst for LO synthesis from the aerobic oxidation of limonene. To assess the intrinsic activity, the initial reaction rates ( $r_i$ ) defined as the number of limonene consumed per gram of catalyst per unit time were calculated under limonene conversion lower than 21.0 %. Not surprisingly, the OVCC offers a higher  $r_i$  value of  $0.0448\text{ mol g}_{\text{cat}}^{-1}\text{ h}^{-1}$



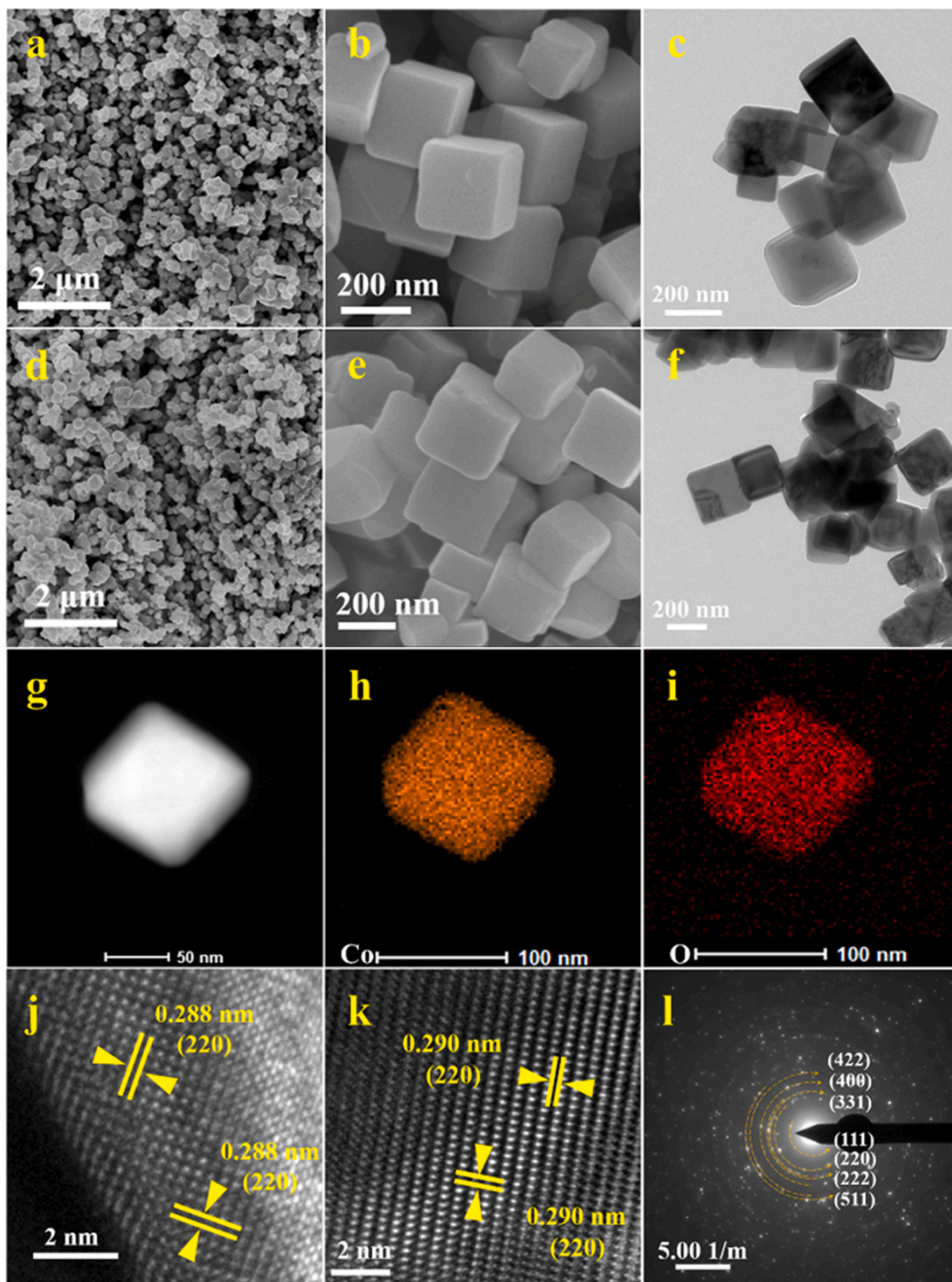


**Fig. 2.** The representative SEM images (a, b) and TEM image (c) of the PCC. Representative SEM images (d, e) and TEM image (f) of the OVCC. (g–i) EDS mapping images of the OVCC. The HRTEM images of the PCC (j) and OVCC (k). The SAED pattern (l) of the OVCC.

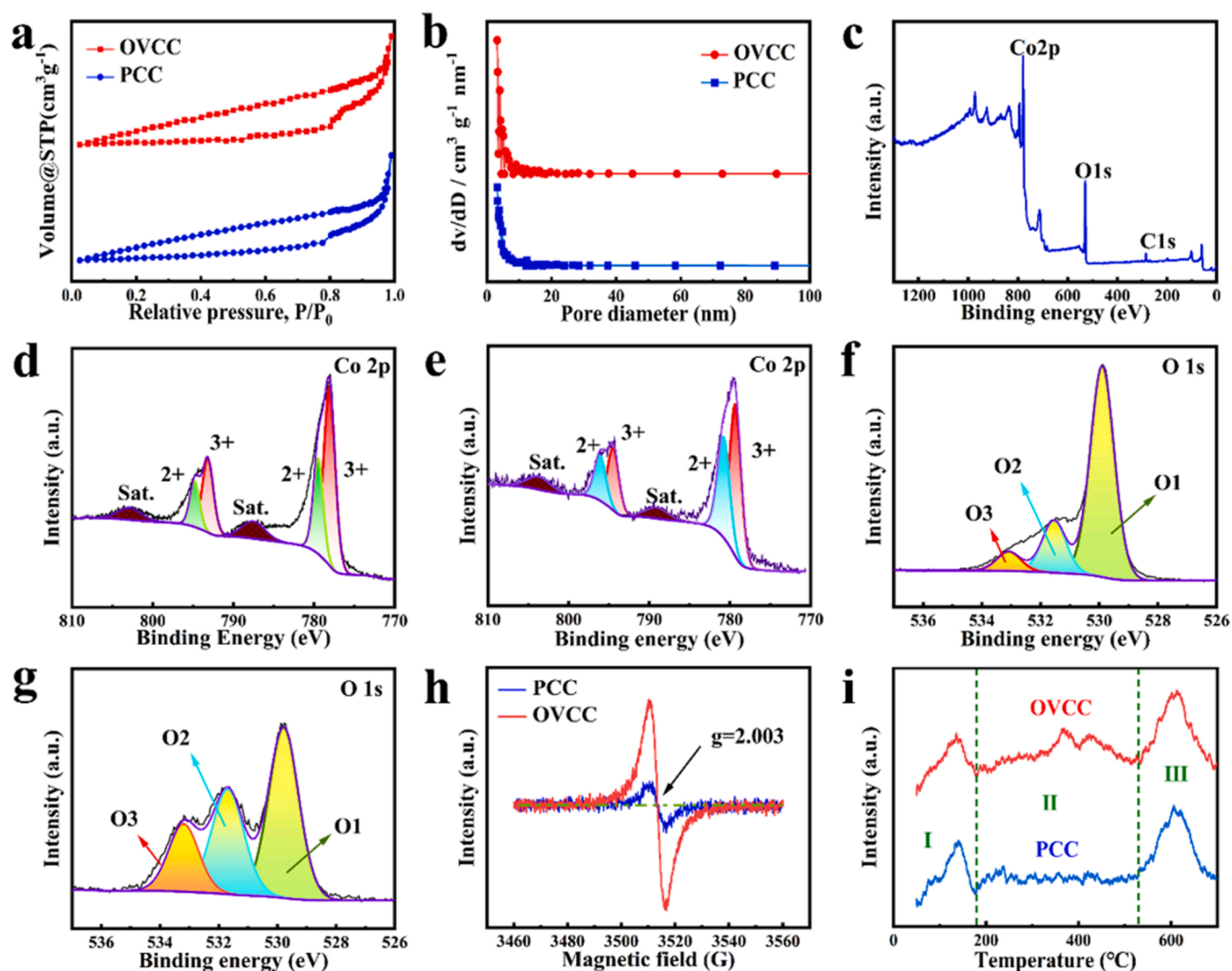
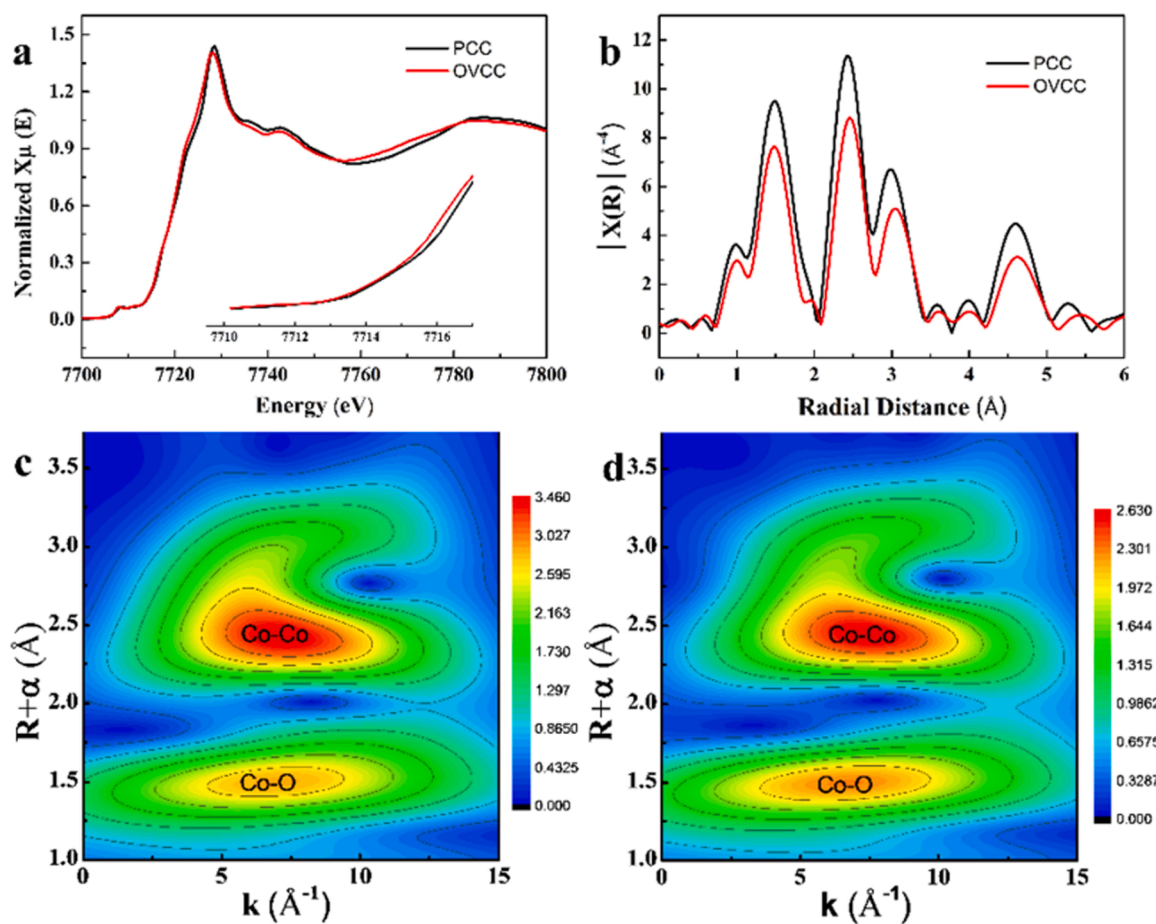


Fig. 3. The  $N_2$  adsorption–desorption isotherms (a) and pore size distributions (b) of the samples. XPS survey (c), high-resolution Co 2p (d) for the PCC and Co 2p (e) for the OVCC, and high-resolution O 1s (f) for the PCC and O 1s (g) for the OVCC. EPR spectra (h) and  $O_2$ -TPD profiles (i) of the samples.

than the PCC ( $0.0333 \text{ mol g}_{\text{cat}}^{-1} \text{ h}^{-1}$ ).

We also explored the effect of reducing condition on the catalytic performance by treating the PCC with other concentrations of ascorbic acid. As listed in Table S1, the concentration of ascorbic acid used for the preparation of the OVCC (0.05 mol/L) is the most appropriate. At concentrations either lower (0.03 mol/L) or higher (0.10 mol/L) for treating the PCC, decrease in the LO yield can be observed. To further reveal the catalytic properties of the OVCC toward limonene oxidation, we have conducted a series of catalytic tests under different reaction conditions catalyzed by the OVCC. These tests were performed at fixed reaction conditions while allowing for only a single reaction variable to be systematically altered. The influence of the reaction temperature was first explored. As displayed in Fig. 5b, the limonene conversion increases with the uphill of the reaction temperature, while the LO selectivity shows the reversing trend with more LDO produced. It can be found the LO yield takes a volcanic trend with the increased reaction temperature. Considering the compromise between the activity and selectivity, the reaction temperature of  $30^\circ\text{C}$  was selected as the optimum parameter for the subsequent work. Fig. 5c presents the catalytic results with different OVCC dosages. In the absence of a catalyst, only 5.8 % conversion of limonene was obtained after 2 h of reaction. With 0.10 g of the OVCC added as the catalyst, the conversion value can achieve 82.3 % with a selectivity to LO of 79.0 %. When the catalyst dosage was increased to 0.15 g, a higher conversion of 87.4 % and almost same LO

selectivity of 79.6 % can be realized. Further increasing the catalyst dosage only witnessed a small increment from 87.4 (0.15 g) to 88.6 % (0.20 g) and then to 89.3 % (0.25 g), while the LO selectivity started to decline obviously from 79.2 % (0.20 g) to 75.6 % (0.25 g). Hence, a catalyst dosage of 0.15 g is suitable in this case. The effect of reaction time was also studied, and the results are exhibited in Fig. 5d. A quick enhancement of the conversion of limonene from 57.6 % at 1 h to 87.4 % at 2 h was acquired. The conversion of limonene progressively increases as the reaction time was prolonged, accompanied with the continuous decrease in the LO selectivity. The reaction duration of 2 h is enough since the LO yield obtained at 3 h (70.2 %) is almost the same with that at 2 h (69.6 %). The reaction pressure is also an importance reaction parameter in the oxidation reaction of hydrocarbons. The limonene oxidation reactions herein were investigated with the oxygen pressure ranging from 0.1 to 0.4 MPa, and the results are summarized in Fig. 5e. It can be found that a higher oxygen pressure affords a higher conversion value but lower selectivity to LO. An oxygen pressure of 0.2 MPa was chosen as an optimum parameter for further research since the changes in the limonene conversion are less marked once the pressure exceeds 0.2 MPa. Finally, the involvement of isobutyraldehyde in the reaction system was probed, and the results are presented in Fig. 5f. In the absence of isobutyraldehyde, the reaction can hardly proceed (only 1.2 % conversion of limonene). Therefore, isobutyraldehyde as a reductant is indispensable for the aerobic oxidation of limonene, as discussed later.



**Fig. 4.** (a) The Co *K*-edge XANES spectra of the samples. Inset, magnified pre-edge XANES region. (b) EXAFS patterns of the samples in *R*-space. WT-EXAFS contour plot of Co *K*-edge signals for the PCC (c) and OVCC (d).

Moreover, the dosage of isobutyraldehyde also presents a significant influence on the limonene oxidation performance. When 5, 10 and 15 mmol of isobutyraldehyde were added to the reaction mixture, the limonene conversion undergoes a quick rise from 7.9 % to 31.3 %, and then to 87.4 %. With a further increase of isobutyraldehyde to 20 mmol, an increment from 87.4 % to 98.5 % can be realized, while the LO selectivity drops dramatically from 79.6 % to 37.9 % (with a concomitant rise of LDO selectivity from 14.7 % to 56.7 %). This can be attributed to the deep oxidation of LO to LDO due to the excessive oxidation capacity of the catalytic system if overdose of isobutyraldehyde was involved in the reaction mixture. Therefore, 15 mmol of isobutyraldehyde (1.875 equiv. of limonene) was selected as the optimal reaction parameter for the OVCC-catalyzed aerobic oxidation of limonene. To sum up, we have systematically explored several key reaction parameters, and the optimum reaction conditions based on these results and findings can be summarized as follows: adopting 0.15 g of the OVCC catalyst in a mixture of 8 mmol of limonene, 10 mL of acetonitrile and 15 mmol of isobutyraldehyde under 0.2 MPa of oxygen at 30 °C for 2 h. Under the optimum conditions, the LO yield achieves 69.6 % with 87.4 % conversion of limonene ( $r_i$  value of  $0.0448 \text{ mol g}_{\text{cat}}^{-1} \text{ h}^{-1}$ ) and 79.6 % selectivity of LO. As listed in Table S2, compared with the reported findings under different reaction systems, the OVCC as a heterogeneous catalyst shows excellent limonene aerobic oxidation performance for producing LO.

Recycling performance is important and essential from the perspectives of industrial application and environmental protection [65, 66]. The recycling performance of the OVCC in limonene oxidation was assessed with a five-time recycle test of 2 h per cycle. As presented in Fig. 6(a, b), no apparent deterioration in the oxidation performance

including catalytic activity and product selectivity was detected. As shown in Fig. S3, the hot-filtration test of the OVCC catalyst demonstrates its heterogeneous nature in the limonene oxidation catalysis. In addition, the ICP–AES characterization was performed to detect the possible metal leaching after reaction, which indicates that no Co detached from the fresh catalyst surface. The XRD (Fig. 6c) and SEM (Fig. S4) characterization results for the OVCC following the recycling performance testing confirm that the crystal structure and morphology are maintained. In addition, the XPS data in Fig. 6(d, e) suggest that the ratios of  $\text{Co}^{2+}/\text{Co}^{3+}$  (0.65) and  $\text{O}2/\text{O}1$  (0.40) are lower than that in the fresh OVCC catalyst, possibly resulting in slight decrease of catalytic activity during the test. All these results verify that the OVCC catalyst is recyclable and stable, further revealing its good application prospect in the aerobic oxidation of limonene to produce LO with high added-value.

### 3.3. Mechanistic insights into boosted catalytic performance

As discussed above, the OVCC and PCC show similar morphology and texture. Therefore, the general physicochemical properties such as surface area, pore structure and grain size can be excluded for the possible contributions to the performance discrepancy of the OVCC and PCC. More specifically, the enhanced activity of the OVCC over the PCC should be intrinsically attributed to the modified surface chemical environment and electronic properties benefited from the defect engineering strategy. To further investigate the origin of the enhanced catalytic activity, additional analyses and experiments were performed. Fig. 6f shows the Arrhenius plots for the PCC and OVCC. The determined apparent activation energy ( $E_a$ ) of the OVCC is  $38.7 \text{ kJ mol}^{-1}$ , lower than that of the PCC ( $42.2 \text{ kJ mol}^{-1}$ ). This implies that the energy



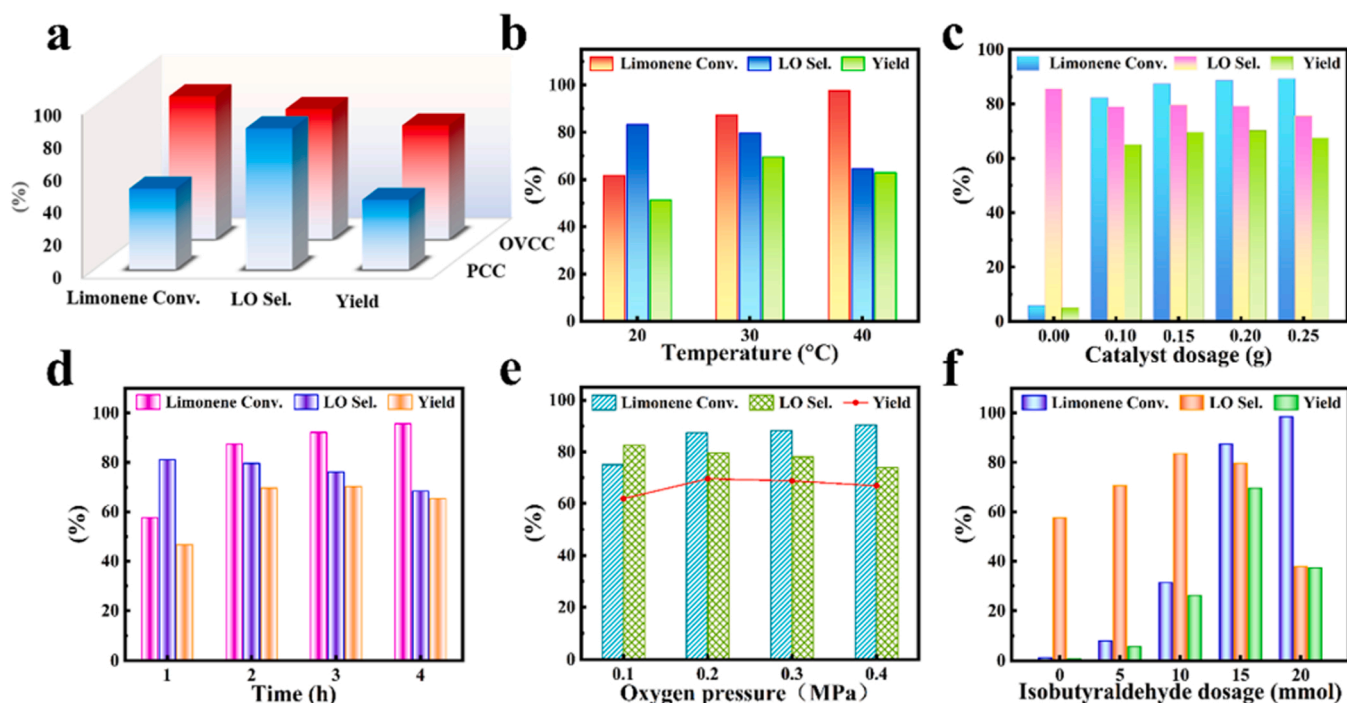


**Fig. 5.** (a) Catalytic performance for the oxidation of limonene of the PCC and OVCC. Reaction conditions: 0.15 g of catalyst, 8 mmol of limonene, 10 mL of acetonitrile, 15 mmol of isobutyraldehyde, 0.2 MPa of oxygen, 30 °C, 2 h. (b) The effect of reaction temperature on the performance; reaction conditions: 0.15 g of OVCC, 8 mmol of limonene, 10 mL of acetonitrile, 15 mmol of isobutyraldehyde, 0.2 MPa of oxygen. (c) The effect of catalyst dosage on the performance; reaction conditions: a certain amount of OVCC catalyst, 8 mmol of limonene, 10 mL of acetonitrile, 15 mmol of isobutyraldehyde, 0.2 MPa of oxygen, 30 °C, 2 h. (d) The effect of reaction duration on the performance; reaction conditions: 0.15 g of OVCC, 8 mmol of limonene, 10 mL of acetonitrile, 15 mmol of isobutyraldehyde, 0.2 MPa of oxygen, 30 °C. (e) The effect of oxygen pressure on the performance; reaction conditions: 0.15 g of OVCC, 8 mmol of limonene, 10 mL of acetonitrile, 15 mmol of isobutyraldehyde, 30 °C, 2 h, a certain pressure of oxygen. (f) The effect of isobutyraldehyde dosage on the performance; reaction conditions: 0.15 g of catalyst, 8 mmol of limonene, 10 mL of acetonitrile, 0.2 MPa of oxygen, 30 °C, 2 h, a certain amount of isobutyraldehyde.

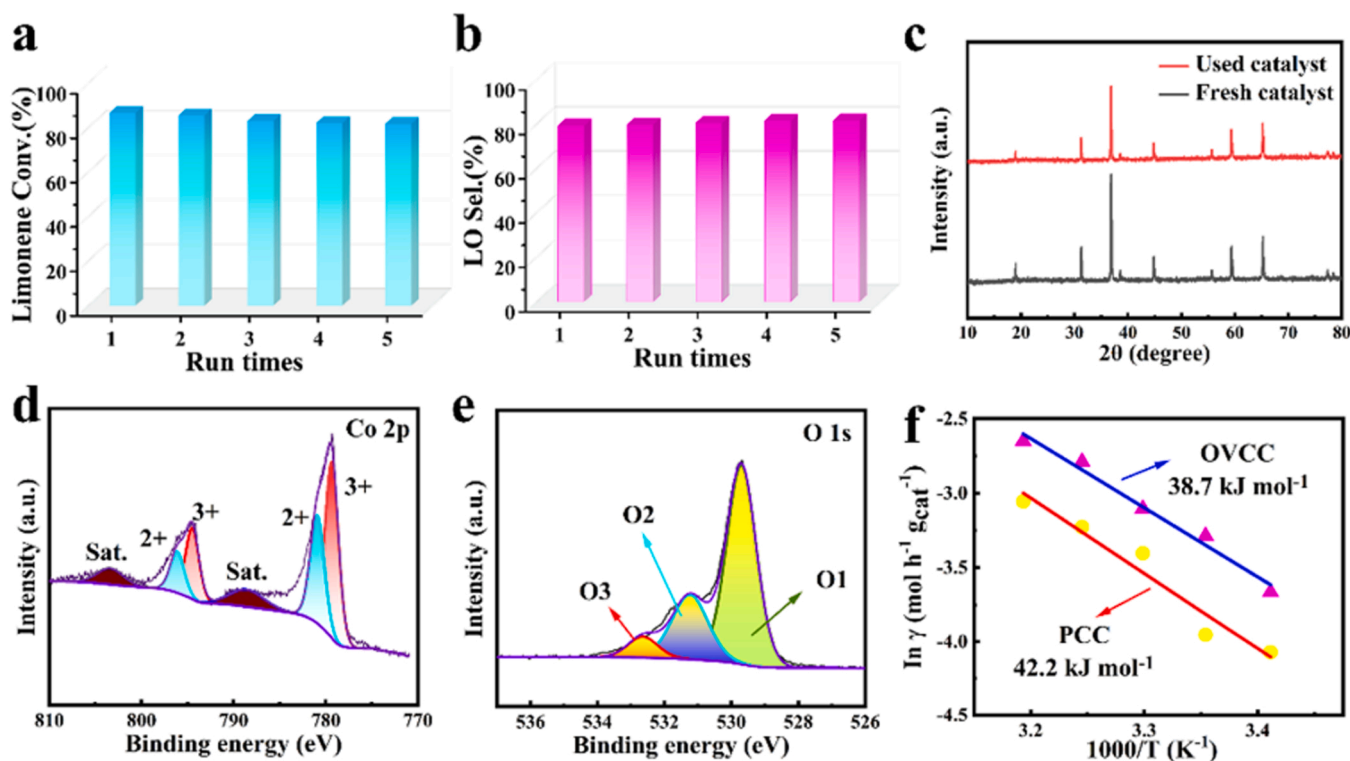


**Fig. 6.** (a, b) The recycling test of the OVCC catalyst. Reaction conditions: 0.15 g of fresh or recovered OVCC, 8 mmol of limonene, 10 mL of acetonitrile, 15 mmol of isobutyraldehyde, 0.2 MPa of oxygen, 30 °C, 2 h. The XRD pattern (c) and high-resolution XPS Co 2p (d) and O 1s (e) spectra of the spent OVCC catalyst. (f) The Arrhenius plots for the samples in the limonene oxidation reaction.

required for limonene oxidation over the OVCC with abundant Ov can be reduced, which benefits from the defect engineering strategy.

Fig. 7a summarizes the reaction results of a series of control experiments. The reaction can hardly proceed in the absence of isobutyraldehyde or using  $N_2$  instead of  $O_2$ . Hence, the involvement of isobutyraldehyde and  $O_2$  in the reaction system is indispensable for driving the aerobic oxidation of limonene. The molecular oxygen is the primary source of oxygen for limonene oxidation and isobutyraldehyde as a reductant assists in activating molecular oxygen which is difficult to be directly activated due to the triplet ground state of  $O_2$ . In fact, the isobutyraldehyde/ $O_2$  system has been substantiated to be a feasible way for selective oxidation of hydrocarbons under mild reaction conditions [67,68]. Moreover, a calcination treatment of the OVCC at 300 °C for 0.5 h in air was performed, and the obtained sample was denoted as OVCC-CT. When applied for the oxidation of limonene under the same reaction conditions, the OVCC-CT shows a conversion of only 52.1 %, which is remarkably lower than the OVCC (87.4 %) and even slightly lower than the PCC (52.7 %). Noticeably, the EPR signal at  $g$  of 2.003 for the OVCC-CT is markedly lower than that of the OVCC (Fig. S5), suggesting the decrease of Ov after the calcination treatment. This finding firmly confirms the vital importance of Ov in boosting the generation of active oxygen species for limonene oxidation catalysis.

To further probe the contribution of reactive oxygen species for the oxidation of limonene, the radical quenching experiments were performed. As presented in Fig. 7b, the reaction was completely shut down

when 2,2,6,6-tetramethylpiperidine-1-oxyl (TEMPO) was added in the standard reaction, demonstrating a radical-mediated nature of the OVCC-catalyzed limonene oxidation [69,70]. The addition of tert-butanol has almost no inhibition effect on the reaction since the limonene conversion was kept nearly unchanged (86.3 % vs. 87.4 %). This suggests that  $\bullet OH$  is barely involved in the limonene oxidation reaction. Significantly, the reaction was stopped after the addition of 2, 6-di-tert-butyl-4-methylphenol (BHT) for the capturing of carbon-centered radical [71]. These findings strongly verifies that the aerobic oxidation of limonene over the OVCC mediated by isobutyraldehyde follows a radical reaction mechanism, and the generated isobutyryl radical is indeed present in the reaction system. In addition, the addition of  $p$ -benzoquinone (PBQ) witnessed a decline in the limonene conversion from 87.4 % to 39.6 %, suggesting that  $\bullet O_2^-$  also has a partial contribution to the oxidation of limonene.

Based on these results and analyses, a plausible reaction mechanism for the OVCC-catalyzed limonene oxidation in the presence of molecular oxygen and isobutyraldehyde can be speculated as presented in Fig. 7c, which consists of two reaction pathways. In pathway I, the reaction is initiated by the formation of isobutyryl radical via the hydrogen-atom abstraction from an isobutyraldehyde molecule under the catalysis of  $Co^{II}-OV$  sites. The subsequent combination of isobutyryl radical and  $O_2$  produces isobutyryl peroxy radical which abstracts a hydrogen-atom from another isobutyraldehyde molecule, resulting in the generation of isobutyl peroxyacid and another isobutyryl radical. The oxidation of

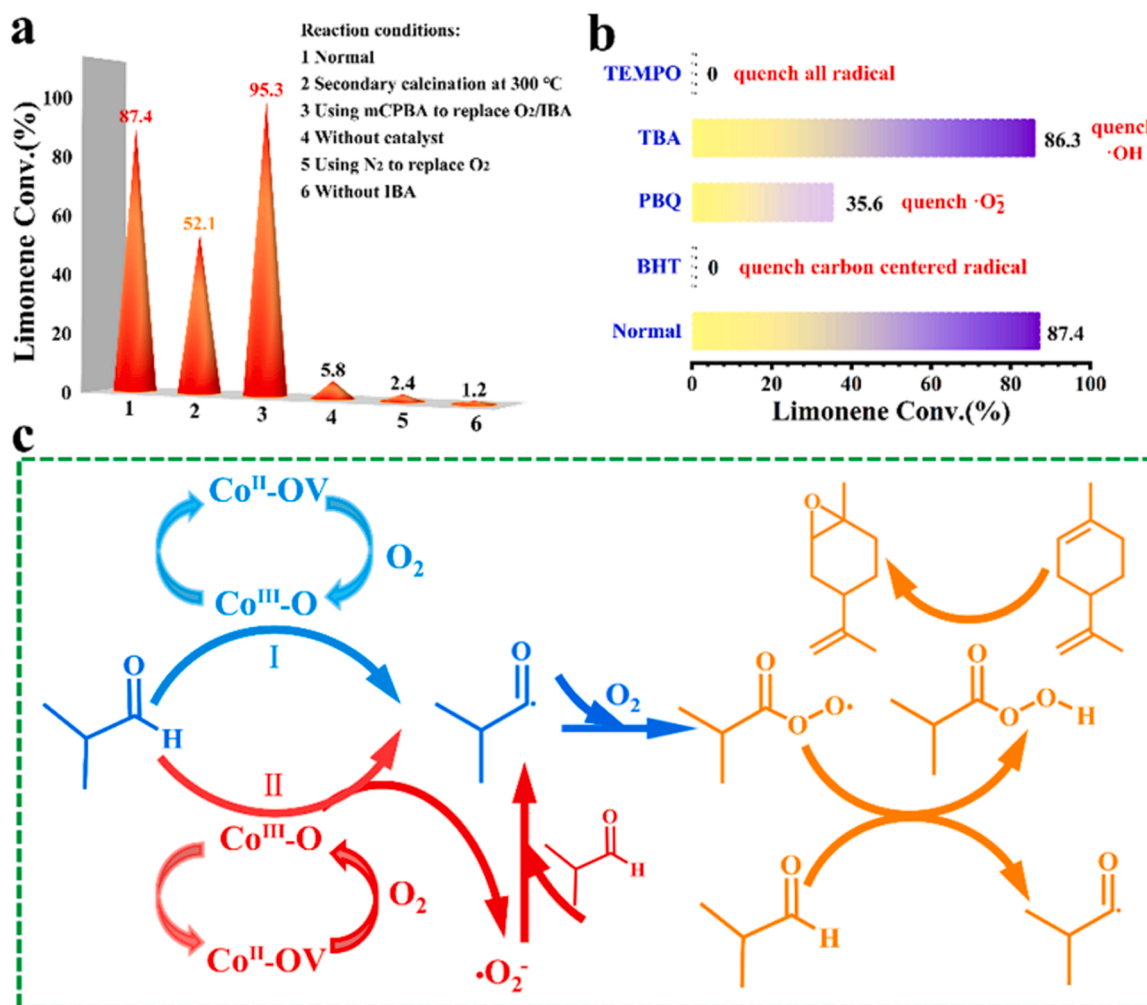


Fig. 7. (a) A series of control experiments for revealing the origin of enhanced performance for the OVCC-catalyzed limonene oxidation. mCPBA:  $m$ -chloroperoxybenzoic acid; IBA: isobutyraldehyde. (b) Active radicals quenching experiments for oxidation of limonene catalyzed by the OVCC. (c) Proposed reaction pathway for the OVCC-catalyzed limonene oxidation.

limonene is finally triggered with the help of isobutyl peroxyacid with high oxidation ability. In pathway II, isobutyraldehyde and  $O_2$  can be activated for the generation of isobutyryl radical and  $\bullet O_2^-$ . The active  $\bullet O_2^-$  radical further trigger the oxidation of isobutyraldehyde to isobutyryl radical which will take part in the whole catalytic cycle.

Additional experiments can be performed to verify the key role of isobutyl peroxyacid in the reaction. When *m*-chloroperoxybenzoic acid was added into the reaction system (Fig. 7a), high conversions of limonene were realized whether the OVCC catalyst was involved or not, which manifests the vital role of peroxy acid in driving the limonene oxidation catalysis. Furthermore, the formation of isobutyl peroxyacid in the reaction system was detected by adding ABTS (2,2'-azino-bis(3-ethylbenzthiazoline-6-sulfonic acid) diammonium salt) solution into the reaction mixture after 0.5 h of reaction (Fig. S6), which produced a green coloured intermediate [72]. All these findings firmly substantiate the proposed reaction pathway.

DFT calculations were carried out to further rationalize the enhanced catalytic oxidation performance of limonene on the  $Co_3O_4$  nanocubes with Ov defects. Due to the dominantly exposed (100) nanocrystalline planes in the  $Co_3O_4$  cubes of the PCC and OVCC, the generation of active species in the initial stage of both the pathway I and pathway II were compared on the (100) surface of the  $Co_3O_4$  model with or without the involvement of oxygen vacancies. Fig. 8 presents the computational

results including the optimized geometric structures (Fig. 8(a, b)) and the corresponding energy profiles (Fig. 8(c, d)). It can be seen from Fig. 8a and c that the Ov in  $Co_3O_4$  benefits the formation of isobutyryl radical through H abstraction from isobutyraldehyde molecule. Fig. 8b and d shows that both active  $\bullet O_2^-$  and isobutyryl radical species can be more easily formed on the Ov-containing surface. This indicates both the reaction pathways I and II as illustrated in Fig. 7 are facilitated by the Ov-containing (100) surface. Thus, the introduction of Ov in  $Co_3O_4$  can steer the radical initiation process through more efficient routes, boosting the production of more active isobutyryl and  $\bullet O_2^-$  radicals. This accounts for the superior activity of defective  $Co_3O_{4-x}$  to that of  $Co_3O_4$ . Hence, the theoretical results are in well consistency with the experimental findings, illustrating that by creating Ov defects in the  $Co_3O_4$  structure, the limonene oxidation kinetics and intrinsic reaction activity can be remarkably facilitated.

#### 4. Conclusion

In summary, we have developed  $Co_3O_4$  nanocubes enriched with Ov via a facile liquid-phase reduction treatment, which can be employed as an efficient catalyst for the aerobic oxidation of limonene. Under the optimum conditions, the LO yield achieves 69.6 % with 87.4 % conversion of limonene ( $r_1$  value of  $0.0448 \text{ mol g}_{\text{cat}}^{-1} \text{ h}^{-1}$ ) and 79.6 %

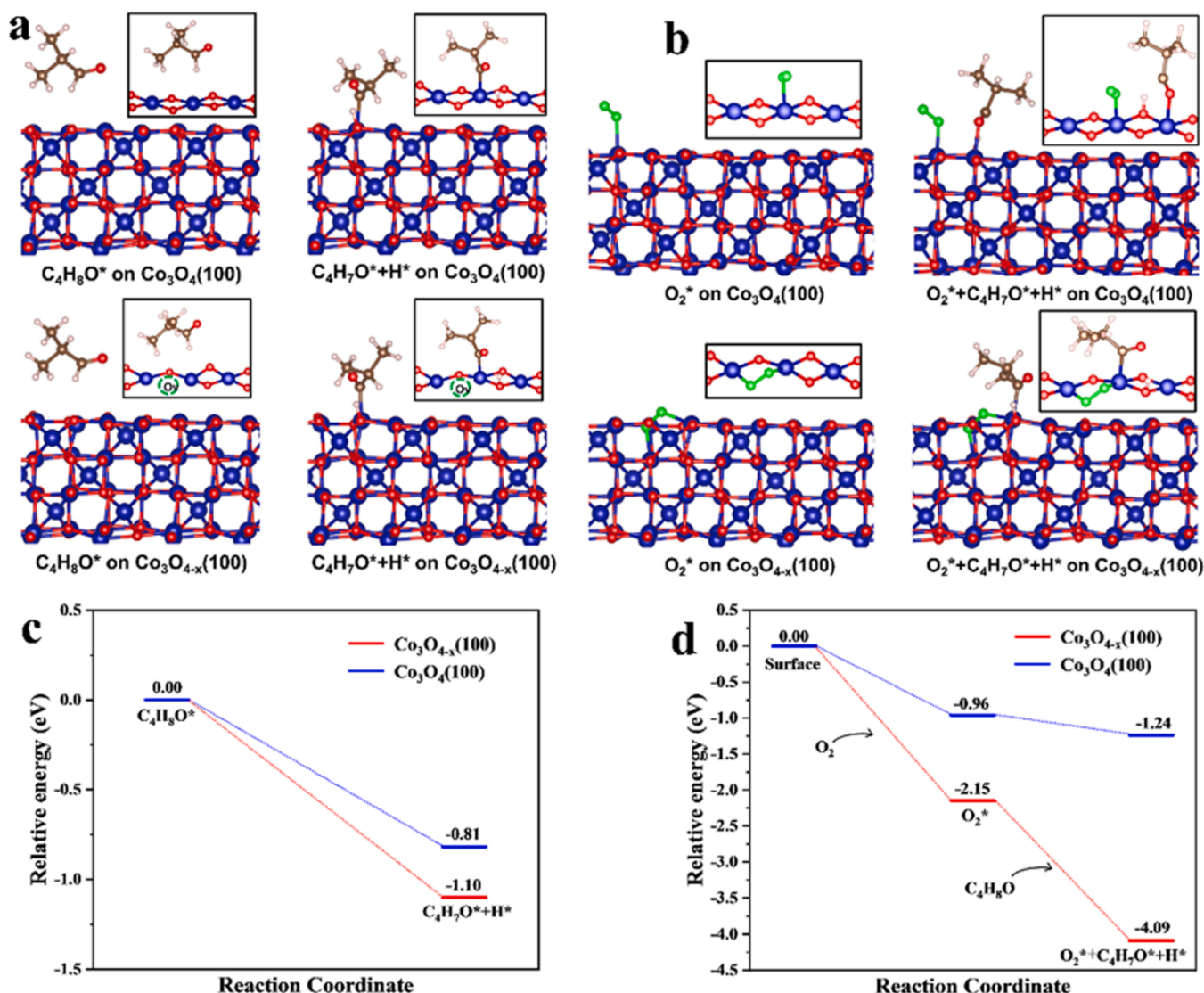


Fig. 8. DFT calculations for the generation of active species in the initial stage of pathway I (a, c) and pathway II (b, d).



selectivity of LO. Systematical experimental findings and theoretical calculation results substantiate the regulation of the local coordination environment and electronic structure induced by the oxygen-vacancy defect engineering strategy, which promotes the production of active species and accelerates the limonene oxidation kinetics and intrinsic reaction activity. In addition with the superior reaction performance, the OVCC catalyst possesses the merits of robust stability, cost effectiveness and easy scale-up capacity, endowing it a promising prospect for the oxidation of limonene for fine chemical synthesis.

### CRedit authorship contribution statement

**Jiangyong Liu:** Conceptualization, Methodology, Formal analysis, Funding acquisition, Project administration, Resources, Supervision, Validation, Writing – review & editing. **Hui Tang:** Data curation, Investigation, Methodology, Software, Visualization, Writing – review & editing. **Panming Jian:** Supervision, Resources, Writing – review & editing. **Bing Liu:** Data curation, Software, Formal analysis, Validation, Writing – review & editing.

### Declaration of Competing Interest

The authors declare that they have no known competing financial interests or personal relationships that could have appeared to influence the work reported in this paper.

### Data Availability

Data will be made available on request.

### Acknowledgements

This work was supported by the National Natural Science Foundation of China (22208284) and the Natural Science Foundation of Jiangsu Province (BK20200956). The authors acknowledge the Priority Academic Program Development of Jiangsu Higher Education Institutions.

### Appendix A. Supporting information

Supplementary data associated with this article can be found in the online version at doi:10.1016/j.apcatb.2023.122828.

### References

- [1] S. Li, L. Rong, S. Wang, S. Liu, Z. Lu, L. Miao, B. Zhao, C. Zhang, D. Xiao, K. Pushpanathan, A. Wong, A. Yu, Enhanced limonene production by metabolically engineered *Yarrowia lipolytica* from cheap carbon sources, *Chem. Eng. Sci.* 249 (2022), 117342.
- [2] W.B. Cunningham, J.D. Tibbetts, M. Hutchby, K.A. Maltby, M.G. Davidson, U. Hintermair, P. Plucinski, S.D. Bull, Sustainable catalytic protocols for the solvent free epoxidation and anti-dihydroxylation of the alkene bonds of biorenewable terpene feedstocks using  $H_2O_2$  as oxidant, *Green Chem.* 22 (2020) 513–524.
- [3] L. Charbonneau, X. Foster, S. Kaliaguine, Ultrasonic and catalyst-free epoxidation of limonene and other terpenes using dimethyl dioxirane in semibatch conditions, *ACS Sustain. Chem. Eng.* 6 (2018) 12224–12231.
- [4] S. Madadi, J.-Y. Bergeron, S. Kaliaguine, Kinetic investigation of aerobic epoxidation of limonene over cobalt substituted mesoporous SBA-16, *Catal. Sci. Technol.* 11 (2021) 594–611.
- [5] J. Cubillos, S. Vázquez, C. Montes, de Correa, Salen manganese (III) complexes as catalysts for R-(+)-limonene oxidation, *Appl. Catal. A* 373 (2010) 57–65.
- [6] A.D. Silva, M.L. Patitucci, H.R. Bizzo, E. D'Elia, O.A.C. Antunes, Wacker  $PdCl_2$ - $CuCl_2$  catalytic oxidation process: oxidation of limonene, *Catal. Commun.* 3 (2002) 435–440.
- [7] D. Naróg, A. Szczepaniak, A. Sobkowiak, Iron(II, III)-catalyzed oxidation of limonene by dioxygen, *Catal. Lett.* 120 (2008) 320–325.
- [8] S. Borocci, F. Marotti, G. Mancini, D. Monti, A. Pastorini, Selectivity in the oxidation of limonene by amphiphilized metalloporphyrins in micellar media, *Langmuir* 17 (2001) 7198–7203.
- [9] N.K. Kala Raj, V.G. Puranik, C. Gopinathan, A.V. Ramaswamy, Selective oxidation of limonene over sodium salt of cobalt containing sandwich-type polyoxotungstate  $[WCo_3(H_2O)_2(W_9CoO_{34})_2]^{10-}$ , *Appl. Catal. A* 256 (2003) 265–273.
- [10] W. Wang, D. Agustin, R. Poli, Influence of ligand substitution on molybdenum catalysts with tridentate Schiff base ligands for the organic solvent-free oxidation of limonene using aqueous TBHP as oxidant, *Mol. Catal.* 443 (2017) 52–59.
- [11] P. Oliveira, A. Machado, A.M. Ramos, I.M. Fonseca, F.M. Braz Fernandes, A. M. Botelho do Rego, J. Vital, Anchoring manganese acetylacetonate complex on MCM-41: Catalytic testing on limonene oxidation, *Catal. Commun.* 8 (2007) 1366–1372.
- [12] P. Oliveira, A.M. Ramos, I. Fonseca, A. Botelho do Rego, J. Vital, Oxidation of limonene over carbon anchored transition metal Schiff base complexes: effect of the linking agent, *Catal. Today* 102–103 (2005) 67–77.
- [13] S.G. Casuscelli, M.E. Crivello, C.F. Perez, G. Ghione, E.R. Herrero, L.R. Pizzio, P. G. Vázquez, C.V. Cáceres, M.N. Blanco, Effect of reaction conditions on limonene epoxidation with  $H_2O_2$  catalyzed by supported Keggin heteropolycompounds, *Appl. Catal. A* 274 (2004) 115–122.
- [14] L.S. Yuan, S. Chandren, J.O.N. Efendi, C.S. Ho, H. Nur, Hydrophobic effect of silica functionalized with silylated Ti-salicylaldehyde complex on limonene oxidation by aqueous hydrogen peroxide, *J. Chem. Sci.* 127 (2015) 1905–1917.
- [15] J.-A. Becerra, A.-L. Villa, Thermodynamic Analysis of  $\alpha$ -Pinene and Limonene Allylic Oxidation over a  $FePcCl_{16}$ -NH $_2$ -SiO $_2$  Catalyst, *Chem. Eng. Technol.* 41 (2018) 124–133.
- [16] C.K. Modi, J.A. Chudasama, H.D. Nakum, D.K. Parmar, A.L. Patel, Catalytic oxidation of limonene over zeolite-Y entrapped oxovanadium (IV) complexes as heterogeneous catalysts, *J. Mol. Catal. A: Chem.* 395 (2014) 151–161.
- [17] D.R. Godhani, H.D. Nakum, D.K. Parmar, J.P. Mehta, N.C. Desai, Zeolite Y encaged Ru(III) and Fe(III) complexes for oxidation of styrene, cyclohexene, limonene, and  $\alpha$ -pinene: An eye-catching impact of  $H_2SO_4$  on product selectivity, *J. Mol. Catal. A: Chem.* 426 (2017) 223–237.
- [18] L. Saikia, D. Srinivas, P. Ratnasamy, Chemo-, regio- and stereo-selective aerial oxidation of limonene to the endo-1,2-epoxide over Mn(Salen)-sulfonated SBA-15, *Appl. Catal. A* 309 (2006) 144–154.
- [19] P. Oliveira, A. Machado, A.M. Ramos, I. Fonseca, F.M.B. Fernandes, A.M. Botelho do Rego, J. Vital, MCM-41 anchored manganese salen complexes as catalysts for limonene oxidation, *Microporous Mesoporous Mater.* 120 (2009) 432–440.
- [20] V.M. Vaschetti, G.A. Eimer, A.L. Cânepa, S.G. Casuscelli, Catalytic performance of V-MCM-41 nanocomposites in liquid phase limonene oxidation: vanadium leaching mitigation, *Microporous Mesoporous Mater.* 311 (2021), 110678.
- [21] A. Wróblewska, J. Serafin, A. Gawarecka, P. Miądlicki, K. Urbaś, Z.C. Koren, J. Llorca, B. Michalkiewicz, Carbonaceous catalysts from orange pulp for limonene oxidation, *Carbon Lett.* 30 (2020) 189–198.
- [22] K. Glonek, A. Wróblewska, E. Makuch, B. Ulejczyk, K. Krawczyk, R.J. Wróbel, Z. C. Koren, B. Michalkiewicz, Oxidation of limonene using activated carbon modified in dielectric barrier discharge plasma, *Appl. Surf. Sci.* 420 (2017) 873–881.
- [23] S. Madadi, S. Kaliaguine, Activated carbon-supported ruthenium as a catalyst for the solvent- and initiator-free aerobic epoxidation of limonene, *ACS Sustain. Chem. Eng.* 9 (2021) 10557–10568.
- [24] J. Bussi, A. López, F. Peña, P. Timbal, D. Paz, D. Lorenzo, E. Dellacasa, Liquid phase oxidation of limonene catalyzed by palladium supported on hydrotalcites, *Appl. Catal. A* 253 (2003) 177–189.
- [25] Z. Strassberger, E.V. Ramos-Fernandez, A. Boonstra, R. Jorna, S. Tanase, G. Rothenberg, Synthesis, characterization and testing of a new  $V_2O_5/Al_2O_3$ -MgO catalyst for butane dehydrogenation and limonene oxidation, *Dalton Trans.* 42 (2013) 5546–5553.
- [26] A. Wróblewska, E. Makuch, J. Młodzik, Z.C. Koren, B. Michalkiewicz, Fe/nanoporous carbon catalysts obtained from molasses for the limonene oxidation process, *Catal. Lett.* 147 (2017) 150–160.
- [27] J. Młodzik, A. Wróblewska, E. Makuch, R.J. Wróbel, B. Michalkiewicz, Fe/EuroPh catalysts for limonene oxidation to 1,2-epoxylimonene, its diol, carveol, carvone and perillyl alcohol, *Catal. Today* 268 (2016) 111–120.
- [28] J. Li, Z. Li, G. Zi, Z. Yao, Z. Luo, Y. Wang, D. Xue, B. Wang, J. Wang, Synthesis, characterizations and catalytic allylic oxidation of limonene to carvone of cobalt doped mesoporous silica templated by reed leaves, *Catal. Commun.* 59 (2015) 233–237.
- [29] M.V. Cagnoli, S.G. Casuscelli, A.M. Alvarez, J.F. Bengoa, N.G. Gallegos, M. E. Crivello, E.R. Herrero, S.G. Marchetti, Ti-MCM-41 silylation: Development of a simple methodology for its estimation: Silylation effect on the activity and selectivity in the limonene oxidation with  $H_2O_2$ , *Catal. Today* 107–108 (2005) 397–403.
- [30] A. Gawarecka, A. Wróblewska, Limonene oxidation over Ti-MCM-41 and Ti-MWW catalysts with t-butyl hydroperoxide as the oxidant, *React. Kinet., Mech. Catal.* 124 (2018) 523–543.
- [31] A. Wróblewska, E. Makuch, P. Miądlicki, The studies on the limonene oxidation over the microporous TS-1 catalyst, *Catal. Today* 268 (2016) 121–129.
- [32] Z. Shi, C. Zhang, C. Tang, N. Jiao, Recent advances in transition-metal catalyzed reactions using molecular oxygen as the oxidant, *Chem. Soc. Rev.* 41 (2012) 3381–3430.
- [33] J. Liu, H. Wang, L. Wang, P. Jian, X. Yan, Phase-dependent catalytic performance of  $MnO_2$  for solvent-free oxidation of ethylbenzene with molecular oxygen, *Appl. Catal. B* 305 (2022), 121050.
- [34] G. Kresse, J. Furthmüller, Efficient iterative schemes for ab initio total-energy calculations using a plane-wave basis set, *Phys. Rev. B* 54 (1996) 11169.
- [35] G. Kresse, J. Furthmüller, Efficiency of ab-initio total energy calculations for metals and semiconductors using a plane-wave basis set, *Comput. Mater. Sci.* 6 (1996) 15–50.
- [36] S.L. Dudarev, G.A. Botton, S.Y. Savrasov, C. Humphreys, A.P. Sutton, Electron-energy-loss spectra and the structural stability of nickel oxide: An LSDA+U study, *Phys. Rev. B* 57 (1998) 1505.

- [37] S. Grimme, J. Antony, S. Ehrlich, H. Krieg, A consistent and accurate ab initio parametrization of density functional dispersion correction (DFT-D) for the 94 elements H-Pu, *J. Chem. Phys.* 132 (2010), 154104.
- [38] P.E. Blöchl, Projector augmented-wave method, *Phys. Rev. B* 50 (1994) 17953.
- [39] J.P. Perdew, K. Burke, M. Ernzerhof, Generalized gradient approximation made simple, *Phys. Rev. Lett.* 77 (1996) 3865.
- [40] G. Yan, P. Sautet, Surface Structure of  $\text{Co}_3\text{O}_4$  (111) under reactive gas-phase environments, *ACS Catal.* 9 (2019) 6380–6392.
- [41] X. Liu, C.T. Prewitt, High-temperature X-ray diffraction study of  $\text{Co}_3\text{O}_4$ : transition from normal to disordered spinel, *Phys. Chem. Miner.* 17 (1990) 168–172.
- [42] H. Liu, W. Long, W. Song, J. Liu, F. Wang, Tuning the electronic bandgap: an efficient way to improve the electrocatalytic activity of carbon-supported  $\text{Co}_3\text{O}_4$  nanocrystals for oxygen reduction reactions, *Chem. Eur. J.* 23 (2017) 2599–2609.
- [43] Z. Cai, Y. Bi, E. Hu, W. Liu, N. Dwarica, Y. Tian, X. Li, Y. Kuang, Y. Li, X.-Q. Yang, H. Wang, X. Sun, Single-crystalline ultrathin  $\text{Co}_3\text{O}_4$  nanosheets with massive vacancy defects for enhanced electrocatalysis, *Adv. Energy Mater.* 8 (2018), 1701694.
- [44] J. Liu, X. Ji, J. Shi, L. Wang, P. Jian, X. Yan, D. Wang, Experimental and theoretical investigation of the tuning of electronic structure in  $\text{SnO}_2$  via Co doping for enhanced styrene epoxidation catalysis, *Catal. Sci. Technol.* 12 (2022) 1499–1511.
- [45] J. Liu, R. Meng, P. Jian, R. Jian,  $\text{CeO}_2$  nanoparticle-decorated  $\text{Co}_3\text{O}_4$  microspheres for selective oxidation of ethylbenzene with molecular oxygen under solvent- and additive-free conditions, *ACS Sustain. Chem. Eng.* 8 (2020) 16791–16802.
- [46] M. Aadil, S. Zulfiqar, M. Shahid, S. Haider, I. Shakir, M.F. Warsi, Binder free mesoporous Ag-doped  $\text{Co}_3\text{O}_4$  nanosheets with outstanding cyclic stability and rate capability for advanced supercapacitor applications, *J. Alloy. Compd.* 844 (2020), 156062.
- [47] Q. Zhao, Y. Zheng, C. Song, Q. Liu, N. Ji, D. Ma, X. Lu, Novel monolithic catalysts derived from in-situ decoration of  $\text{Co}_3\text{O}_4$  and hierarchical  $\text{Co}_3\text{O}_4/\text{MnO}_x$  on Ni foam for VOC oxidation, *Appl. Catal. B* 265 (2020), 118552.
- [48] J. Bae, D. Shin, H. Jeong, C. Choe, Y. Choi, J.W. Han, H. Lee, Facet-dependent Mn doping on shaped  $\text{Co}_3\text{O}_4$  crystals for catalytic oxidation, *ACS Catal.* 11 (2021) 11066–11074.
- [49] J. Liu, R. Meng, H. Wang, P. Jian, Boosting styrene epoxidation via  $\text{CoMn}_2\text{O}_4$  microspheres with unique porous yolk-shell architecture and synergistic intermetallic interaction, *J. Colloid Interface Sci.* 579 (2020) 221–232.
- [50] D. Shen, Z. Li, J. Shan, G. Yu, X. Wang, Y. Zhang, C. Liu, S. Lyu, J. Li, L. Li, Synergistic Pt-CeO<sub>2</sub> interface boosting low temperature dry reforming of methane, *Appl. Catal. B* 318 (2022), 121809.
- [51] J. Liu, W. Wang, L. Wang, P. Jian, Heterostructured  $\text{V}_2\text{O}_5/\text{FeVO}_4$  for enhanced liquid-phase epoxidation of cyclooctene, *J. Colloid Interface Sci.* 630 (2023) 804–812.
- [52] L. Yang, S. Hou, S. Zhu, Z. Shi, X. Wang, J. Jiang, Y. Chu, J. Bai, Y. Wang, L. Zhang, Z. Jiang, C. Liu, W. Xing, J. Ge, Stabilizing Pt electrocatalysts via introducing reducible oxide support as reservoir of electrons and oxygen species, *ACS Catal.* 12 (2022) 13523–13532.
- [53] J. Liu, W. Wang, P. Jian, L. Wang, X. Yan, Promoted selective oxidation of ethylbenzene in liquid phase achieved by hollow  $\text{CeVO}_4$  microspheres, *J. Colloid Interface Sci.* 614 (2022) 102–109.
- [54] H. Yang, L. Jia, Z. Zhang, B. Xu, Z. Liu, Q. Zhang, Y. Cao, Z. Nan, M. Zhang, T. Ohno, Novel cerium-based MOFs photocatalyst for photocatalytic collaborative performance under visible light, *J. Catal.* 405 (2022) 74–83.
- [55] P. Liu, Y. Liao, J. Li, L. Chen, M. Fu, P. Wu, R. Zhu, X. Liang, T. Wu, D. Ye, Insight into the effect of manganese substitution on mesoporous hollow spinel cobalt oxides for catalytic oxidation of toluene, *J. Colloid Interface Sci.* 594 (2021) 713–726.
- [56] Y. Su, K. Fu, Y. Zheng, N. Ji, C. Song, D. Ma, X. Lu, R. Han, Q. Liu, Catalytic oxidation of dichloromethane over Pt-Co/HZSM-5 catalyst: Synergistic effect of single-atom Pt,  $\text{Co}_3\text{O}_4$ , and HZSM-5, *Appl. Catal. B* 288 (2021), 119980.
- [57] W. Zhu, X.-b Wang, C. Li, X. Chen, W.-y Li, Z. Liu, C. Liang, Defect engineering over  $\text{Co}_3\text{O}_4$  catalyst for surface lattice oxygen activation and boosted propane total oxidation, *J. Catal.* 413 (2022) 150–162.
- [58] C. He, Y. Liao, C. Chen, D. Xia, Y. Wang, S. Tian, J. Yang, D. Shu, Realizing a redox-robust Ag/MnO<sub>2</sub> catalyst for efficient wet catalytic ozonation of S-VOCs: Promotional role of Ag(0)/Ag(I)-Mn based redox shuttle, *Appl. Catal. B* 303 (2022), 120881.
- [59] B. Xu, Q. Zhang, S. Yuan, S. Liu, M. Zhang, T. Ohno, Synthesis and photocatalytic performance of yttrium-doped  $\text{CeO}_2$  with a hollow sphere structure, *Catal. Today* 281 (2017) 135–143.
- [60] Z. Li, Y. Zhang, Y. Feng, C.-Q. Cheng, K.-W. Qiu, C.-K. Dong, H. Liu, X.-W. Du,  $\text{Co}_3\text{O}_4$  nanoparticles with ultrasmall size and abundant oxygen vacancies for boosting oxygen involved reactions, *Adv. Funct. Mater.* 29 (2019), 1903444.
- [61] S. Liu, W. Xue, Y. Ji, W. Xu, W. Chen, L. Jia, T. Zhu, Z. Zhong, G. Xu, D. Mei, F. Su, Interfacial oxygen vacancies at  $\text{Co}_3\text{O}_4$ - $\text{CeO}_2$  heterointerfaces boost the catalytic reduction of NO by CO in the presence of O<sub>2</sub>, *Appl. Catal. B* 323 (2023), 122151.
- [62] Y. Lu, T. Liu, C.-L. Dong, C. Yang, L. Zhou, Y.-C. Huang, Y. Li, B. Zhou, Y. Zou, S. Wang, Tailoring competitive adsorption sites by oxygen-vacancy on cobalt oxides to enhance the electrooxidation of biomass, *Adv. Mater.* 34 (2022), 2107185.
- [63] Y. Zhang, S. Zhang, J. Ma, A. Huang, M. Yuan, Y. Li, G. Sun, C. Chen, C. Nan, Oxygen vacancy-rich  $\text{RuO}_2$ - $\text{Co}_3\text{O}_4$  nanohybrids as improved electrocatalysts for Li-O<sub>2</sub> batteries, *ACS Appl. Mater. Interfaces* 13 (2021) 39239–39247.
- [64] R. Li, X. Shi, Y. Huang, M. Chen, D. Zhu, W. Ho, J. Cao, S. Lee, Catalytic oxidation of formaldehyde on ultrathin  $\text{Co}_3\text{O}_4$  nanosheets at room temperature: effect of enhanced active sites exposure on reaction path, *Appl. Catal. B* 319 (2022), 121902.
- [65] J. Liu, R. Meng, J. Li, P. Jian, L. Wang, R. Jian, Achieving high-performance for catalytic epoxidation of styrene with uniform magnetically separable  $\text{CoFe}_2\text{O}_4$  nanoparticles, *Appl. Catal. B* 254 (2019) 214–222.
- [66] J. Liu, H. Wang, R. Ye, P. Jian, L. Wang, Promotional effect of Mn-doping on the catalytic performance of NiO sheets for the selective oxidation of styrene, *J. Colloid Interface Sci.* 585 (2021) 61–71.
- [67] A. Maity, S.-M. Hyun, D.C. Powers, Oxidase catalysis via aerobically generated hypervalent iodine intermediates, *Nat. Chem.* 10 (2018) 200–204.
- [68] Q. Yue, Y. Lu, Z. Zhang, H. Tian, H. Wang, X. Li, S. Liu,  $\text{H}_5\text{PV}_2\text{Mo}_{10}\text{O}_{40}$  encapsulated into  $\text{Cu}_3(\text{BTC})_2$  as an efficient heterogeneous nanocrystalline catalyst for styrene epoxidation, *New J. Chem.* 44 (2020) 16913–16920.
- [69] M. Li, L. Ma, L. Luo, Y. Liu, M. Xu, H. Zhou, Y. Wang, Z. Li, X. Kong, H. Duan, Efficient photocatalytic epoxidation of styrene over a quantum-sized  $\text{SnO}_2$  on carbon nitride as a heterostructured catalyst, *Appl. Catal. B* 309 (2022), 121268.
- [70] K. Zhang, H. Chen, Y. Liu, J. Deng, L. Jing, A. Rastegarpanah, W. Pei, Z. Han, H. Dai, Two-dimensional  $\text{Bi}_2\text{W}_x\text{Mo}_{1-x}\text{O}_6$  solid solution nanosheets for enhanced photocatalytic toluene oxidation to benzaldehyde, *Appl. Catal. B* 315 (2022), 121545.
- [71] X. Cao, Z. Chen, R. Lin, W.-C. Cheong, S. Liu, J. Zhang, Q. Peng, C. Chen, T. Han, X. Tong, Y. Wang, R. Shen, W. Zhu, D. Wang, Y. Li, A photochromic composite with enhanced carrier separation for the photocatalytic activation of benzylic C-H bonds in toluene, *Nat. Catal.* 1 (2018) 704–710.
- [72] M. Gong, Y. Guo, D. Malko, J. Rubio-Garcia, J.M.S. Dawson, G.J.P. Britovsek, A. Kucernak, Using molecular oxygen and Fe-N/C heterogeneous catalysts to achieve Mukaiyama epoxidations via in situ produced organic peroxy acids and acylperoxy radicals, *Catal. Sci. Technol.* 12 (2022) 2978–2989.